Dynamics of the Layered Circulation Inferred from Kinetic Energy Pathway in the South China Sea

ZHONGYA CAI[a,b] AND JIANPING GAN[a]

[a] *Center for Ocean Research in Hong Kong and Macau, Department of Ocean Science and Department of Mathematics, Hong Kong University of Science and Technology, Hong Kong, China*
[b] *State Key Laboratory of Internet of Things for Smart City and Department of Civil and Environmental Engineering, University of Macau, Macau, China*

ABSTRACT: We investigated the mean kinetic energy (MKE) and eddy kinetic energy (EKE) in the South China Sea to illustrate the dynamics of the vertically rotating cyclonic–anticyclonic–cyclonic (CAC) circulation in the upper, middle, and deep layers. We found that strong MKE along the basin slope and the associated EKE arising from the vertical shear and stratification of the mean current characterize the circulation. In the upper layer, the external MKE input from the Kuroshio intrusion and wind forcing drive the cyclonic circulation, with the wind forcing providing most of the EKE. External forcing, however, does not directly provide the MKE and EKE of the CAC circulation in the semi-enclosed middle and deep layers, where the internal pressure work near Luzon Strait and the vertical buoyancy flux (VBF) in the southern basin and along the western slope maintain the MKE and EKE. The internal pressure work is formed by ageostrophic motion and pressure gradient field associated with circulation. The VBF is generated by vertical motion induced by the geostrophic cross-isobath transport along the slope where variable density field is maintained by the external flow and the internal mixing. The kinetic energy pathway in the CAC circulation indicates that the external forcing dominates upper-layer circulation and the coupling between internal and external dynamics is crucial for maintaining the circulation in the middle and deep layers. This study provides a new interpretation to the maintenance of CAC circulation from energy prospect.

KEYWORDS: Ageostrophic circulations; Kinetic energy; Ocean circulation; Ocean dynamics; Pressure

1. Introduction

The South China Sea (SCS) is the largest marginal sea in the tropics (Fig. 1). It has a deep basin, a shallow broad shelf on the west side of its northern and southern parts, and a steep continental slope in its eastern and western basins. Taiwan Strait connects the SCS to the East China Sea, and Luzon Strait (LS) connects the SCS to the Pacific Ocean. Mindoro Strait and Karimata Strait connect the SCS to the Sulu Sea and to the Java Sea, respectively. LS is the only deep channel (~2500 m), and the other three straits are much shallower.

Using Stokes' theorem, Gan et al. (2016a) physically recognized the vertically rotating three-layer cyclonic–anticyclonic–cyclonic (CAC) circulation in the SCS basin. The seasonal Asian monsoon and the Kuroshio intrusion through LS drive the upper-layer mean cyclonic circulation (Yang et al. 2002; Su 2004; Xue et al. 2004; Gan et al. 2006; Fang et al. 2009; Qu et al. 2009; Xu and Oey 2014, Gan et al. 2016a,b). Hydrographic data and numerical simulations show that there are anticyclonic and cyclonic flows along the basin slope in the middle and deep layers, respectively (Yuan 2002; Qu et al. 2006; Wang et al. 2011; Lan et al. 2013, 2015; Shu et al. 2014; Zhu et al. 2017). Vorticity dynamics were widely used to reveal how the CAC circulation forms, but mainly focused on the influence of external forcing on the mean basin circulation. These vorticity studies showed that the external layered

inflow–outflow–inflow through LS provides the positive–negative–positive planetary vorticity flux for the mean CAC circulation in the three different layers (Yang and Price 2000; Lan et al. 2013; Gan et al. 2016a,b; Zhu et al. 2017; Quan and Xue 2018).

While, it has been noticing that the external forcing through LS and internal vertical coupling jointly control how the CAC circulation in the SCS forms and how the circulation is sustained (Cai and Gan 2019). These joint dynamics involve geostrophic motions, nonlinear advection, and mixing processes. Intense turbulent mixing in SCS maintains the density/pressure difference between the basin and the Pacific Ocean, which further contributes to the flow exchange through LS in the deep and middle layers (e.g., Zhao et al. 2014; Wang et al. 2017). The flow exchange through LS is highly nonlinear (Gan et al. 2006; Nan et al. 2015). Inside the basin, the geostrophic cross-isobath transport over the meandering bottom slope, which is the intrinsic response to the external forcing, establishes the vertical coupling between the adjacent layers (Quan and Xue 2019; Cai and Gan 2020). Furthermore, the tidally induced dissipation that amplifies over the rough slope topography (Chang et al. 2006; Tian et al. 2009; Wang et al. 2016) is the possible mechanism that can alter the cross-layer exchange of momentum and vertically link the layers of the CAC circulation (Liu and Gan 2017). However, how all these different processes interact to maintain the layered circulation in the SCS has yet to be adequately addressed.

Analyzing the energy of the system can provide a new way to quantify the contributions from external forcing and internal

Corresponding author: Jianping Gan, magan@ust.hk

FIG. 1. Location and bathymetry (m) of the South China Sea, showing Luzon Strait, Taiwan Strait, Mindoro Strait, and Karimata Strait.

coupling processes. For many purposes, the kinetic energy represents the most direct characteristic of fluid motion, transport properties, and mixing rates of a system (Ferrari and Wunsch 2009). In regional oceans, the energetic analysis can provide understanding of the energy distribution and the conversion between the eddy and mean flows (e.g., Greatbatch et al. 2010; Cessi et al. 2014; Kang and Curchitser 2015; Chen et al. 2016; Magalhães et al. 2017). Generally, the eddy component of kinetic energy (EKE) is greater than the mean kinetic energy (MKE) (e.g., Wyrtki et al. 1976; Richardson 1983; Ferrari and Wunsch 2009). The EKE can come from the release of the MKE through barotropic instability and the release of potential energy through baroclinic instability, both of which are stored in large-scale circulation built up under wind and external forcing.

For the SCS, previous analysis of the energetics mainly focused on the characteristics of surface EKE, which is generally high southeast of Vietnam and southwest of Taiwan Island near LS (e.g., Chen et al. 2009; Cheng and Qi 2010). Yang et al. (2013) showed that the surface EKE (in upper 200 m) can acquire energy from baroclinic instability, barotropic instability, and the external energy flux. How the different processes interact and the associated kinetic energy pathway that sustains the CAC circulation still requires further investigation.

This study presents the three-dimensional characteristics and pathway of kinetic energy in the CAC circulation. With the employment of the energetic analysis, we evaluated the contribution of external forcing and the internal responses of the CAC circulation, examined the importance of the interaction

between the geostrophic motion and ageostrophic processes, and illustrated the dynamics of the CAC circulation from the perspective of the kinetic energy pathway. This paper is organized as follows: section 2 introduces the numerical model and the kinetic energy analysis methods, section 3 shows the three-dimensional structure of the MKE and EKE in CAC circulation, and section 4 presents our detailed investigation of the energy pathway. Discussion of the underlying dynamic processes of the CAC circulation and our conclusions are in sections 5 and 6, respectively.

2. Numerical model and energy equation

For the analysis, we used the results from the China Sea Multiscale Ocean Modeling System (CMOMS) (Gan et al. 2016b), which is based on the Regional Ocean Modeling System (ROMS) (Shchepetkin and McWilliams 2005). CMOMS has already been employed to investigate the layered circulation and water movement within the SCS (Gan et al. 2016a,b; Liu and Gan 2017; Cai and Gan 2020).

CMOMS's domain covers the North Pacific Ocean and all the China Seas from approximately 0.958°N, 99.8°E in the southwest corner to the northeast corner of the Sea of Japan. The model's horizontal resolution is about 0.18°, and the model has 30 vertical levels over its stretched terrain following coordinates. CMOMS nests with the global model of the Ocean General Circulation Model for the Earth Simulator (OFES) (Masumoto et al. 2004), and it includes tidal and subtidal forcing along the open boundaries using a novel open boundary condition (Liu and Gan 2016). We initialized the model

with the *WOA13* hydrographic field and spun up the model for 50 years with climatological atmospheric and lateral fluxes until the model reached a quasi-steady state. We used the last 5 years of daily output for our study. The model results have been rigorously validated with field measurements, satellite remote sensing data, and principles of geophysical fluid dynamics (Gan et al. 2016b). The fact that the model realistically captures the circulation and forcing conditions of the SCS established a high level of confidence in the results of this study.

We derived the equations for computing MKE and EKE to examine the kinematic energy dynamics of the CAC circulation. We divided the velocity $\mathbf{V} = u\mathbf{i} + v\mathbf{j} + w\mathbf{k}$ into temporal mean and perturbated parts: $\mathbf{V} = \overline{\mathbf{V}} + \mathbf{V}'$, where the overbar indicates the time average over a given period, and the prime indicates the eddy state. In this study, we used the annual mean for our time average. For the hydrostatic condition we only considered the horizontal kinetic energy, and we defined mean kinetic energy (MKE; $\overline{E}$) and eddy kinetic energy (EKE; E'), as follows:

$$\begin{cases} \overline{E} = \dfrac{1}{2}\rho_0(\overline{u}^2 + \overline{v}^2) \\ E' = \dfrac{1}{2}\rho_0(\overline{u'^2} + \overline{v'^2}) \end{cases}. \tag{1}$$

Similarly, the calculated density via equation of state in the model can be separated as

$$\rho(x, y, z, t) = \rho_r(z) + \rho_a(x, y, z, t), \tag{2}$$

where ρ_r is the reference density as a function of depth, which we chose to be the time mean and basin-averaged density. Parameter ρ_a is the corresponding anomaly of the density (perturbated part), which varies spatially and temporally (Kang and Curchitser 2015). Like the density, we divided the pressure into reference and perturbated parts:

$$P(x, y, z, t) = P_r(z) + P_a(x, y, z, t). \tag{3}$$

The horizontal momentum equations are

$$\begin{cases} \dfrac{\partial u}{\partial t} + \mathbf{V} \cdot \nabla u - fv = -\dfrac{1}{\rho_0}\dfrac{\partial P}{\partial x} + \mathrm{VIS}_u \\ \dfrac{\partial v}{\partial t} + \mathbf{V} \cdot \nabla v + fu = -\dfrac{1}{\rho_0}\dfrac{\partial P}{\partial y} + \mathrm{VIS}_v \end{cases} \tag{4}$$

in which $\mathbf{V} = u\mathbf{i} + v\mathbf{j} + w\mathbf{k}$ is the velocity, f is the Coriolis parameter, P and ρ_0 represent the pressure and density (set as 1025 kg m^{-3}), VIS_u and VIS_v represent the vertical viscous terms in x and y directions. The horizontal viscosity is relatively small and is included in the vertical viscosity for simplicity. Then, to obtain the governing equation for the MKE, we multiplied Eq. (4) by $\rho_0\overline{u}$ and $\rho_0\overline{v}$ and took the time average of their sum (Kang and Curchitser 2015), to get

$$\frac{\partial \overline{E}}{\partial t} = \overbrace{-\nabla \cdot (\overline{\mathbf{V}}\,\overline{E})}^{\mathrm{DIV\_MKE}} \underbrace{-\overline{\mathbf{V}} \cdot \nabla \overline{P_a}}_{\mathrm{PW}_M} \overbrace{-\rho_0[\overline{u}\nabla \cdot (\overline{\mathbf{V}'u'}) + \overline{v}\nabla \cdot (\overline{\mathbf{V}'v'})]}^{\mathrm{BTI}_M} \underbrace{-g\overline{\rho_a}\,\overline{w}}_{\mathrm{VBF}_M} + \rho_0\overline{\mathbf{V}} \cdot \overline{\mathbf{VIS}} \tag{5a}$$

in which w is the vertical velocity, g is the gravity acceleration, and $\mathbf{VIS} = \mathbf{i}\mathrm{VIS}_u + \mathbf{j}\mathrm{VIS}_v$ represents the vertical viscosity. The other variables are the same as in Eq. (4). The first two terms on the right-hand side are the divergence of the MKE flux (DIV_MKE) and the mean pressure work (PW$_M$) in three-dimensional divergence form, respectively. The third term indicates the changes of MKE caused by the nonlinear interaction between the mean and perturbed flows or barotropic instability (BTI$_M$). The fourth term is the MKE input from the mean vertical buoyancy flux (VBF$_M$) or the mean baroclinic instability. The upward buoyancy flux induced by the upwelling/downwelling of the lighter/denser seawater with $-\overline{\rho_a}/+\overline{\rho_a}$ will release the available potential energy (APE), while the reverse vertical flux converts MKE to APE. The last term in Eq. (5a) represents the effect of vertical viscosity. To explicitly show the kinetic energy input from wind forcing and examine the contributions from different processes in each layer, we vertically integrated Eq. (5a) over all the layers so that we expressed the last term as

$$\int_{\mathrm{layer}} \rho_0\overline{\mathbf{V}} \cdot \overline{\mathbf{VIS}}\, dz = \overbrace{\overline{\mathbf{V}}_s \cdot \overline{\boldsymbol{\tau}}_s}^{\mathrm{WP}_M} + \mathrm{VIS}_M, \tag{5b}$$

in which the $\mathbf{V}_s$ is the surface horizontal velocity and $\boldsymbol{\tau}_s$ is surface wind stress. The WP$_M$ is the MKE input by wind power and VIS$_M$ represents the turbulent viscosity dissipation of MKE in the water column. Below surface in the middle and deep layers, the WP$_M$ disappears and the VIS$_M$ equals to the layer-integrated $\rho_0\overline{\mathbf{V}} \cdot \overline{\mathbf{VIS}}$.

Under the hydrostatic condition, $-g\overline{\rho_a}\,\overline{w} = \overline{w}\partial\overline{P_a}/\partial z$, the net pressure work PW$_M$ is determined by the VBF$_M$ and the horizontal pressure work (PW_H$_M$: $-\overline{\mathbf{V}}_h \cdot \nabla_h\overline{P_a} = -\overline{u}\partial\overline{P_a}/\partial x - \overline{v}\partial\overline{P_a}/\partial y$) so that PW$_M$ = PW_H$_M$ − VBF$_M$. Because the geostrophic motion cannot produce the pressure work, the PW_H$_M$ illustrates the interaction between the ageostrophic motions and the pressure field:

$$\overline{\mathbf{V}}_h \cdot \nabla_h\overline{P_a} = \overline{\mathbf{V}}_{h\_\mathrm{adv}} \cdot \nabla_h\overline{P_a} + \overline{\mathbf{V}}_{h\_\mathrm{vvis}} \cdot \nabla_h\overline{P_a}, \tag{6}$$

where the $\overline{\mathbf{V}}_{h\_\mathrm{adv}}$ and $\overline{\mathbf{V}}_{h\_\mathrm{vvis}}$ represent the horizontal ageostrophic motions induced by the nonlinearity and turbulent viscosity, respectively.

Similarly, we obtained the equation that governs EKE by multiplying the momentum equations in Eq. (4) by ρ_0u' and ρ_0v' and then taking the time average of the sum:

TABLE 1. The energy terms in MKE and EKE equations.

Term	Mathematical form	Physical meaning
DIV_MKE	$-\nabla \cdot (\overline{\mathbf{V}}\,\overline{E})$	Divergence of the MKE flux
PW_M	$\overline{\mathbf{V}} \cdot \nabla \overline{P_a}$	Mean pressure work
PW_H_M	$-\overline{\mathbf{V}}_h \cdot \nabla_h \overline{P_a}$	Horizontal mean pressure work
BTI_M	$-\rho_0[\overline{u}\nabla \cdot (\overline{\mathbf{V}'u'}) + \overline{v}\nabla \cdot (\overline{\mathbf{V}'v'})]$	MKE input due to nonlinear interaction between the mean and perturbed flows
VBF_M	$-g\overline{\rho_a}\,\overline{w}$	Mean vertical buoyancy flux
WP_M	$\overline{\mathbf{V}}_s \cdot \overline{\boldsymbol{\tau}}_s$	Surface wind power input to MKE
VIS_M	$\int_{\text{layer}} \rho_0 \overline{\mathbf{V}} \cdot \overline{\mathbf{VIS}}\,dz - \overline{\mathbf{V}}_s \cdot \overline{\boldsymbol{\tau}}_s$	Turbulent viscosity dissipation of MKE
DIV_EKE	$-\nabla \cdot (\overline{\mathbf{V}E'})$	Divergence of the EKE flux
PW_E	$-(\overline{\mathbf{V} \cdot \nabla P'})$	Eddy pressure work
PW_H_E	$-\overline{\mathbf{V}'_h \cdot \nabla_h P'_a}$	Horizontal eddy pressure work
BTI_E	$-\rho_0[\overline{u'\mathbf{V}'} \cdot \nabla\overline{u} + \overline{v'\mathbf{V}'} \cdot \nabla\overline{v}]$	EKE input due to nonlinear interaction between the mean and perturbed flows
VBF_E	$-g\overline{\rho'_a\,w'}$	Eddy vertical buoyancy flux
WP_E	$\overline{\mathbf{V}'_s \cdot \boldsymbol{\tau}'_s}$	Surface wind power input to EKE
VIS_E	$\int_{\text{layer}} \rho_0 \overline{\mathbf{V}' \cdot \mathbf{VIS}'}\,dz - \overline{\mathbf{V}'_s \cdot \boldsymbol{\tau}'_s}$	Turbulent viscosity dissipation of EKE

$$\frac{\partial E'}{\partial t} = \overbrace{-\nabla \cdot (\overline{\mathbf{V}E'})}^{\text{DIV\_EKE}} \underbrace{-(\overline{\mathbf{V} \cdot \nabla P'})}_{PW_E} \overbrace{-\rho_0[\overline{u'\mathbf{V}'} \cdot \nabla\overline{u} + \overline{v'\mathbf{V}'} \cdot \nabla\overline{v}]}^{BTI_E} \underbrace{-g\overline{\rho'_a\,w'}}_{VBF_E} + \rho_0\overline{\mathbf{V}' \cdot \mathbf{VIS}'} \tag{7}$$

The terms on the right side are the same as the ones in Eq. (5a) except for the EKE's corresponding perturbation components. Similarly, we expressed the layered integration, $\int_{\text{layer}}\rho_0 \overline{\mathbf{V} \cdot \mathbf{VIS}'}\,dz$, as $\overbrace{\overline{\mathbf{V}'_s \cdot \boldsymbol{\tau}'_s}}^{WP_E} + VIS_E$, and the net PW_E in the EKE budget is determined by the VBF_E and the PW_H_E ($-\overline{\mathbf{V}'_h \cdot \nabla_h P'_a}$). The MKE and EKE energy terms used in this study are summarized in Table 1.

3. Energy characteristics of the CAC circulation

We illustrate the energy structure of the CAC circulation using the layer-integrated MKE and EKE (Fig. 2). Based on the definitions for the layers found in Gan et al. (2016a,b), we separated the three layers by the depths of 750 and 1500 m. To illustrate the characteristics of the basin circulation clearly, we excluded the shelf regions where the depths were less than 100 m.

a. Upper layer

The structure and intensity of the MKE directly represents the mean CAC circulation (Figs. 2a–c). The Kuroshio intrusion and basinwide positive wind stress curl drive the upper-layer mean circulation to flow cyclonically with the strong southwestward and southward boundary current along the northern and western slopes of the SCS. Along the northern slope, the MKE is larger near LS due to the direct influence from the Kuroshio intrusion. The MKE intensity gradually decreases southwestwardly and western intensification increases the intensity as the current flows southward along the western boundary. Meridionally,

the upper-layer MKE has two centers with large magnitudes in the northern basin near LS (~21°N) and to the east of Vietnam along the western boundary (12°–15°N) (Figs. 2a and 3a).

The forming EKE is related to perturbations like mesoscale eddies and meandering currents, which are manifestations of the dynamic variabilities that modulate the basin circulation. In the upper layer (Fig. 2d), there is high EKE southwest of Taiwan and southeast of the Vietnam where well-known active eddy areas are (e.g., Wang et al. 2003; Gan and Qu 2008; Chen et al. 2009; Cheng and Qi 2010; Wang et al. 2012). The variabilities in the wind forcing and the Kuroshio intrusion are the major drivers of the variability in the upper layer. Along the northern slope and the northern part of western boundary, the flow is relatively regular with smaller EKE. While the EKE tends to be correlated with the MKE, it is not the case in the southern basin (south of 12°N) with the highest EKE (Fig. 3a), where there is a local cyclonic gyre and seasonal reversing current over a local trough (Gan et al. 2006). The stronger EKE and decorrelation between MKE and EKE suggest that local dynamic processes produce the strong variability in the circulation.

b. Middle layer

In the middle layer, high MKE along the northward western boundary current distinguishes the anticyclonic circulation (Fig. 2b). In the northeastern basin, external Pacific water intrudes into the SCS basin through the northern part of LS, although much weaker than that in the upper layer. The intrusion generates a westward current,
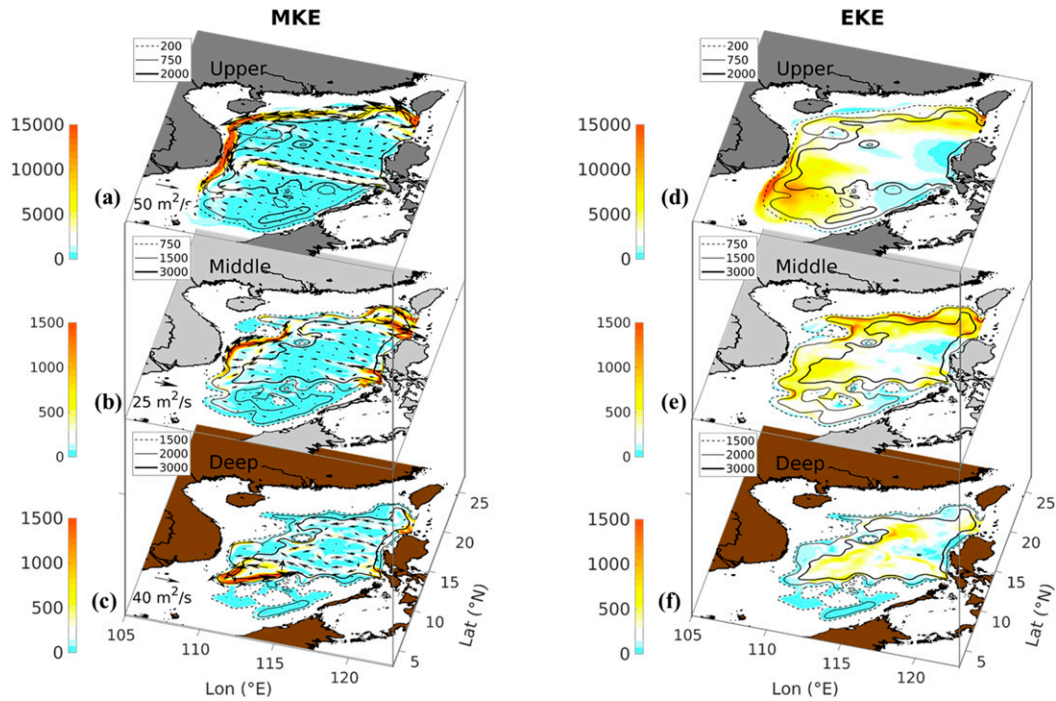
FIG. 2. Horizontal distribution of layer-integrated (a)–(c) MKE (J m^{-2}) and (d)–(f) EKE (J m^{-2}) in the upper, middle, and deep layers. The three layers are separated by 750 and 1500 m. Arrows indicate the depth-integrated velocity in each layer. The dashed, solid, and bold solid lines indicate the isobath lines.

produces a relatively high MKE, and affects the water properties over the northern slope. The basic meridional pattern of middle layer MKE is like the upper layer's MKE that it has two high MKE centers in the northern

basin near LS (18°–21°N) and along the western slope (12°–15°N) (Fig. 3b).

The distribution of the EKE in the middle layer does not relate directly to the intensity of the mean circulation or MKE.
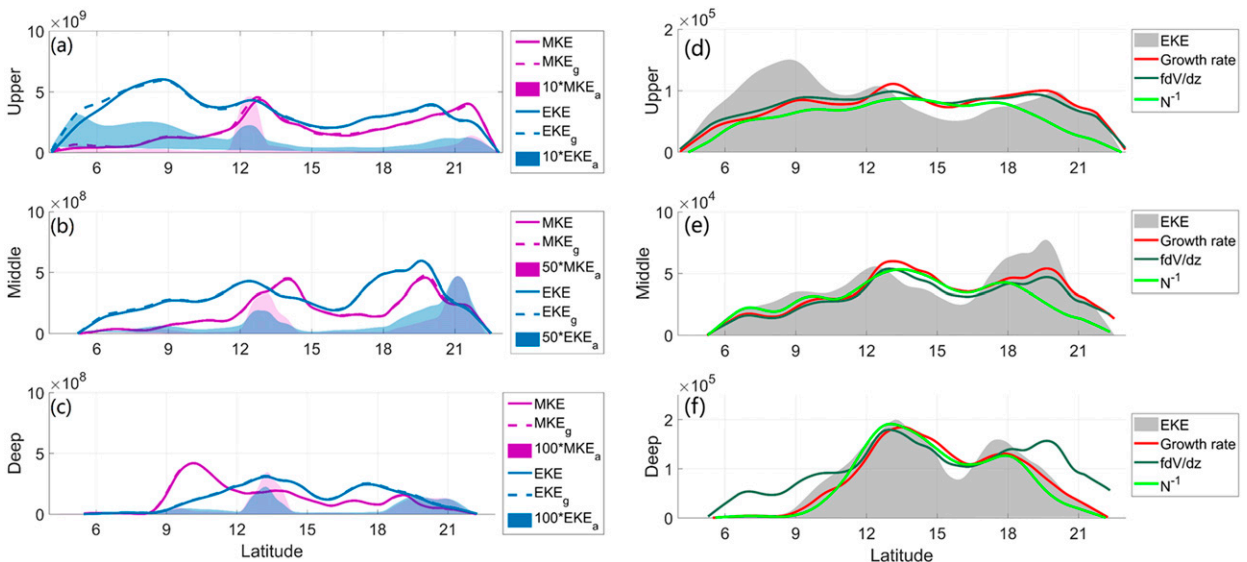

FIG. 3. (a)–(c) Zonal- and layer-integrated MKE (purple lines; J m^{-1}) and EKE (blue lines; J m^{-1}) as a function of latitude in the upper, middle, and deep layers. The dashed lines and the colored shadows indicate the associated geostrophic (MKE$_g$ and EKE$_g$) and ageostrophic components (MKE$_a$ and EKE$_a$), respectively. (d)–(f) Zonal- and layered-integrated baroclinic growth rate σ, vertical shear $f(dV/dz)$, inversed stratification N^{-1}, and EKE. The variables are normalized to have the same scale as σ.

High EKE is mainly produced along the northern slope and in the southwest basin where the MKE is relatively weak. Interestingly, the strong northward current or MKE in the western boundary current does not locally induce large EKE (Fig. 2e). Again, the underlying dynamics for the EKE distribution might be connected to the variability of the layered circulation associated with the local flow interacting with the topography.

c. Deep layer

The strong eddy-like rotating current over the topographic trough in the southwest corner highlights the MKE in the deep layer (Fig. 2c). Although the deep intrusion through LS provides the positive planetary vorticity flux to generate the basin-scale cyclonic circulation, the MKE in the northern and central basin (north of 12°N) is weak (Fig. 3c) relative to the MKE in the upper layer. The difference in the two layers is likely due to the much smaller deep intrusive flux, which is about 6 times smaller than the intrusion into the upper layer (Gan et al. 2016a). Thus, we speculate that the kinetic energy of the cyclonic circulation over the southwest corner is produced from internal processes instead of a direct input from external MKE.

Like the middle layer, the strong slope current over the southwest corner does not generate significant local EKE (Fig. 2f). The large EKE magnitude is mainly in the central (12°–15°N) and northern basins (18°N) where the MKE is relatively small (Fig. 3c).

In all three layers, the geostrophic motions dominate the MKE and EKE (Figs. 3a–c). The ageostrophic components are found mainly along the western slope where there are a strong slope current and steep topography and in the northern basin near LS. Near LS, the exchange current with the Pacific and the eddy shedding associated with the Kuroshio loop current induce the strong nonlinearity (e.g., Gan et al. 2006; Zhang et al. 2017). In addition, internal tides propagate into the SCS basin through LS, which elevate the turbulent mixing near LS and over the basin slope due to the sharp varying topography (Zu et al. 2008; Tian et al. 2009; Alford et al. 2015; Xu et al. 2016; Huang et al. 2016). Those processes could contribute to the stronger ageostrophic component near LS and over the meandering slope in the SCS. In the upper layer, the larger ageostrophic component of the EKE also exists in the southern basin, which is affected by the seasonal reversing circulation and eddies associated with the coastal current separation (Gan and Qu 2008). The intensity of the ageostrophic processes is much weaker than the intensity of the geostrophic motion but plays the crucial role in modulating the kinetic energy in the CAC circulation that we discuss in section 5.

d. Baroclinic growth rate

The MKE affects the EKE but has a different spatial pattern in the three layers, which suggests that there is a contribution from local dynamic processes. To check the spatial characteristics of the EKE in the CAC circulation, we examine the baroclinic growth rate (σ), which plays an important role in the mesoscale eddies that induce EKE (Noh et al. 2007; Stammer 1997; Qiu 1999):

$$\sigma = \frac{f}{N}\frac{dV}{dz}, \tag{8}$$

where N is the Brunt–Väisälä frequency, dV/dz is the vertical shear of the velocity, and f is the Coriolis parameter. The vertical shear produces favorable conditions for perturbation growth, which produces a larger EKE, while the stratification has a negative effect.

As shown in Figs. 3d–f, σ strongly affects the spatial pattern of the EKE, particularly in the semi-enclosed middle and deep layers. In the upper layer, σ mainly correlates to the EKE pattern in the region north of ~12°N. The peak of σ provides favorable conditions for perturbation growth with the energy input from various processes described in section 4a. In the upper and middle layers, the vertical shear $f(dV/dz)$ largely determines σ, and stratification affects σ. In the deep layer, the baroclinic stratification of the background circulation plays the larger role, which is indicative of the internal baroclinic processes contributing more to the energy budget in the deep basin. Consequently, the EKE is not spatially distributed in the same way as the MKE's intensity, particularly in the semi-enclosed middle and deep layers because the internal vertical shear and stratification of the background mean circulation affect how the EKE is distributed.

4. Energy budget

Using Eqs. (5a) and (7), we calculated the budget of the MKE and EKE, then we integrated the budget over the three layers to examine how different processes contributed to the maintenance of CAC circulation (Fig. 4). For simplicity, we focus on the net contributions and the meridional structures in this paper.

a. Upper layer

In the upper layer (Fig. 4a), the MKE of the cyclonic circulation is provided by the surface wind power input (WP$_M$) (40%) and the external Kuroshio intrusion induced MKE flux (DIV_MKE) (60%). What the wind and Kuroshio contribute to the upper-layer circulation is consistent with the findings from the layer-integrated vorticity analysis by Gan et al. (2016a). Besides the turbulent viscosity (VIS$_M$) that dissipates the majority of the MKE, part of the MKE (20%) converts to EKE through the barotropic instability (BTI$_M$) to cascade the energy of the mean circulation. The contributions from the internal pressure work (PW$_M$) and vertical buoyancy flux (VBF$_M$) are relatively small. The wind power input (WP$_E$) (90%) dominates the basin-scale EKE (Fig. 4d), and the turbulent viscosity (VIS$_E$) dissipates the basin-scale EKE. The BTI$_E$ extracts energy from the mean circulation but plays a minor role in providing EKE (6%).

The MKE flux (DIV_MKE) and pressure work (PW$_M$) control the basic meridional MKE pattern in the upper layer, which generally have opposing values and spatial patterns (Fig. 5a). The Kuroshio intrusion-induced positive DIV_MKE generates high MKE in the northern basin, and as the response, the negative PW$_M$ is formed there associated with the setup of the pressure field. The positive DIV_MKE in the north basin
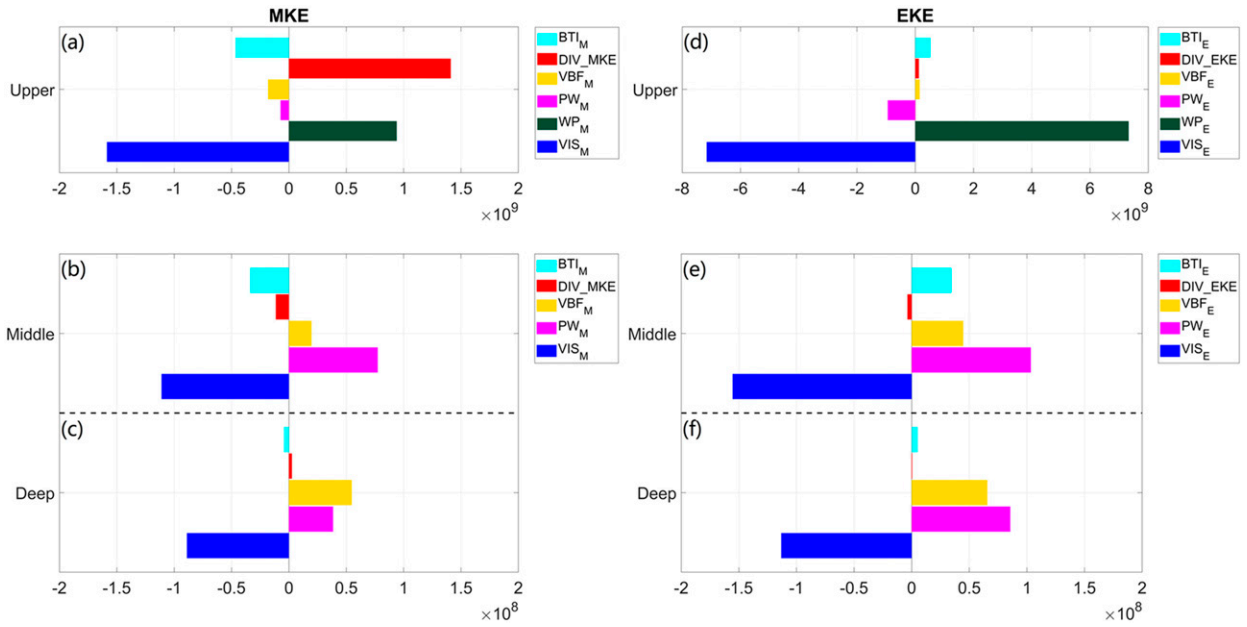
FIG. 4. Contribution of different processes (J s^{-1}) to the budget of (a)–(c) MKE in Eq. (5a) and (d)–(f) EKE in Eq. (7) for the three layers. DIV_MKE: MKE flux; PW$_M$: mean pressure work; BTI$_M$: barotropic instability; VBF$_M$: mean vertical buoyancy flux; WP$_M$: mean wind power input; VIS$_M$: turbulent viscosity dissipation of MKE. Terms in (d)–(f) have the same meanings as the MKE terms but are for the EKE. The upper layer has a different x axis from the middle and deep layers.

also indicates the decrease of MKE as the current flows along the northern slope, as also shown in Fig. 2a. The direct wind power input (WP$_M$) contributes more power in the northern basin, but its role is smaller than DIV_MKE. Along the western boundary (12°–15°N), the PW$_M$, which transports the intruded MKE across the basin, maintains the increase in the MKE associated with the western intensification.

For the EKE, the wind power input (WP$_E$) dominates its meridional structure (Fig. 5d) and produces high EKE in the southern basin and near LS, which also indicates the importance of the viscosity in the EKE dynamics. Inside the basin, the PW$_E$ alternates between positive and negative values to redistribute the internal EKE and acts as the net energy sink.
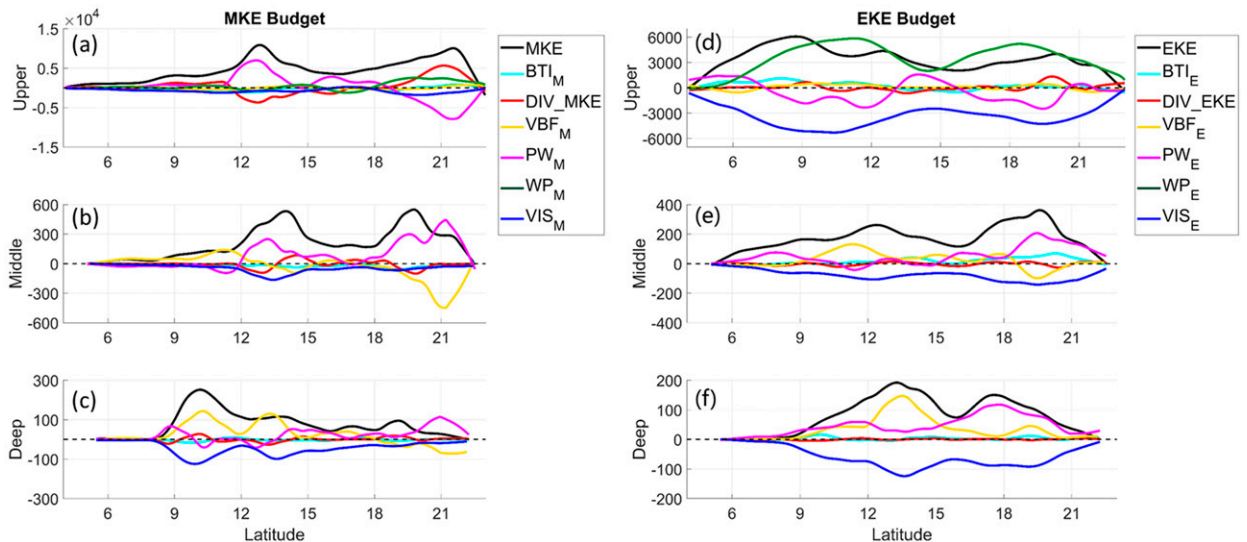

FIG. 5. Zonal- and layer-integrated terms (J m^{-1} s^{-1}) in the (a)–(c) MKE and (d)–(f) EKE equations as a function of latitude in the upper, middle, and deep layers. The zonal- and layered-integrated MKE and EKE were normalized to have the same scale. Each term means the same as it does in Fig. 4.

b. Middle layer

In the middle layer, the outflow through LS does not provide the net MKE input, but acts as the MKE sink (Fig. 4b). The PW_M (80%) mainly provides the MKE of the mean anticyclonic circulation. Inside the basin, the VBF_M releases the APE to maintain the mean circulation (20%). Similar to the upper layer, part of the middle layer MKE (23%) converts into smaller-scale perturbations through BTI_M and VIS_M dissipates the majority part. The middle layer EKE is jointly provided by the pressure work PW_E (57%), internal VBF_E that releases the energy from APE (24%), and the BTI_E that extracts the energy from large-scale mean circulation (19%) (Fig. 4e).

Spatially, it is the positive PW_M, not the direct external MKE input, that generates the high MKE in the northern basin near LS (Fig. 5b). As illustrated in previous studies, the density-induced pressure difference between the SCS basin and the western Pacific affects the middle/deep-layer outflow/inflow (e.g., Zhu et al. 2019), which contributes to the PW_M of the middle-layer circulation. Associated with positive pressure work, part of the MKE converts to the APE through negative VBF_M in the northern basin that is induced by the upwelling of $+\overline{\rho_a}$ water, as we discuss below. The PW_M also exists along the western slope to support the northward slope current of anticyclonic circulation. The release of APE by VBF_M mainly occurs in the southern basin (south of 12°N) and helps maintain the local anticyclonic circulation there.

Associated with the formation of large PW_M, the eddy pressure work (PW_E) is generated and contributes to the high EKE peak along the northern slope (Fig. 5e) where there is a higher baroclinic growth rate. In addition, the EKE extracts energy from the large-scale mean circulation through the BTI_E over the northern slope but generally plays a minor role. Along the western slope, the EKE peak (~12°N) is mainly supported by the internal local VBF_E where there is relatively strong upwelling and VBF_M as we discuss in section 5.

c. Deep layer

In the deep layer (Fig. 4c), the direct external MKE flux (DIV_MKE) caused by deep intrusion contributes very little to the basin cyclonic circulation. Instead, the internal VBF_M (57%) and the PW_M (40%) provide most of the MKE to which the vertical buoyancy flux contributes more. The advective interaction between the mean current and the perturbation (BTI_M) is limited, and the deep layer loses energy due to VIS_M. For the deep layer EKE, its source is generally the same as the middle layer's source, except there is almost no conversion of energy from the mean circulation (Fig. 4f). The internal VBF_E and PW_E account for 42% and 55% of the total EKE input, respectively.

Over the southwest corner, the release of APE through internal VBF_M locally maintains the deep layer strong cyclonic circulation, and the circulation loses energy mainly through VIS_M (Fig. 5c). Thus, the internal density structure and the vertical motion, from the perspective of kinetic energy dynamics, play the key roles in maintaining the cyclonic circulation in the deep layer. For the EKE, the basic meridional energy budget pattern is similar to the middle layer's (Fig. 5f),
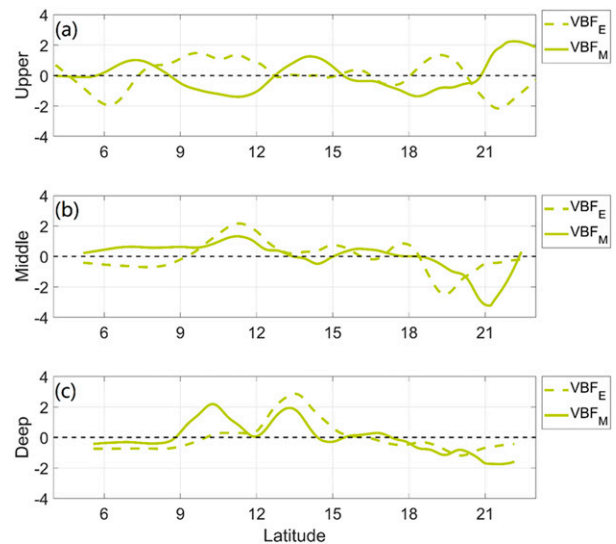

FIG. 6. (a)–(c) Zonal- and layer-integrated VBF_E (dashed lines) and VBF_M (solid lines) as a function of latitude in the upper, middle, and deep layers, respectively. The mean values were removed then normalized by the standard derivation to make the two variables comparable.

and the PW_E and local VBF_E produce the high EKE in the northern basin (~18°N) and central basin (~12°–15°N), respectively. The VIS_E occurs throughout the basin to dissipate the generated EKE.

5. Discussion

The energy budget analysis indicates that the external energy input from the Kuroshio intrusion and the surface wind forcing, which are relatively well understood in the SCS, drives the upper-layer circulation. In the semi-enclosed middle and deep layers, the direct energy input from the external exchange flow is rather limited, and the pressure work (i.e., PW_M and PW_E) and internal vertical buoyancy flux-induced baroclinic instability (i.e., VBF_M and VBF_E) play the major roles in maintaining the layered circulation. In this discussion, we further explore the internal vertical buoyancy flux and the pressure work, which are largely unclear and involve the interaction between the geostrophic and ageostrophic processes in forming the CAC circulation.

a. Vertical buoyancy flux

Generally, the eddy vertical buoyancy flux (VBF_E) is associated with the mean vertical buoyancy flux (VBF_M) in the three layers (Fig. 6). In the upper layer, the VBF_E and VBF_M have opposing meridional variations such that the region with negative/positive VBF_M has positive/negative VBF_E (Fig. 6a). Thus, for the upper-layer circulation, the VBF_E releases the potential energy generated by the upwelling of denser water (to be discussed below). While in the middle and deep layers, the positive peaks of the VBF_E, which maintain the internal high EKE locally, are formed associated with the relatively
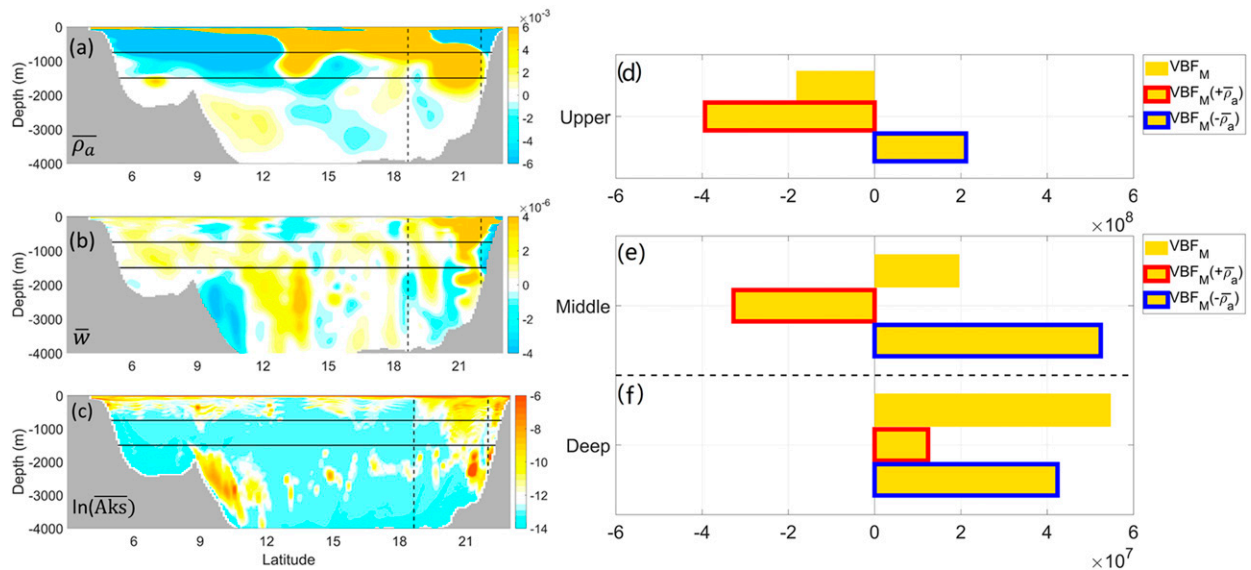
FIG. 7. (a)–(c) Zonally averaged $\overline{\rho_a}$ (kg m^{-3}), $\overline{w}$ (m s^{-1}), and ln($\overline{\text{Aks}}$) as function of depth and latitude. Black solid lines indicate the 750- and 1500-m depths and dashed lines indicate the location of LS. (d)–(f) Magnitude of the mean vertical buoyancy flux (VBF$_M$; J s^{-1}) generated in the regions with $+\overline{\rho_a}$ and $-\overline{\rho_a}$ in the three layers.

high σ (Figs. 4d–f) and the generation of large VBF$_M$ (Figs. 6b,c). The VBF$_E$ and VBF$_M$ occur in phase with a slight spatial shift in the northern part of the middle layer where the negative VBF$_M$ induced by the upwelling of $+\overline{\rho_a}$ water also leads to the negative VBF$_E$.

The three-dimensional motion and associated density flux largely control the formation of VBF$_M$ and VBF$_E$ that release the APE to maintain the MKE and EKE, particularly in the semi-enclosed middle and deep layers. We further examined the zonally averaged $\overline{\rho_a}$, vertical motion $\overline{w}$, and the turbulent mixing intensity $\overline{\text{Aks}}$ in the three layers (Fig. 7). The $\overline{\text{Aks}}$ represents the mean turbulent mixing coefficient used in the simulation of temperature/salinity, which is obtained from turbulence closure model (Mellor and Yamada 1982) in the ROMS.

b. Mean density structure

In the upper layer, the positive $\overline{\rho_a}$ in the central and northern basins indicate the upwelling of the denser water from the middle layer, which is induced by the diverging cyclonic upper-layer circulation and the Ekman pumping of the wind forcing (Fig. 7a). In the northern part of LS, the Kuroshio water is less dense than the Northern SCS and the intrusion induces the negative $\overline{\rho_a}$, despite the intensified vertical mixing and upward $\overline{w}$ there (Figs. 7b,c). The pathway of SCS water, identified from the density distribution, illustrates that, in the upper layer, the upwelling mainly occurs in the northern and western SCS, where there is positive $\overline{\rho_a}$ (Liu and Gan 2017). Similarly, Fig. 7d shows that the upper-layer negative VBF$_M$ that converts MKE to the potential energy is mainly induced by the upwelling of the denser water in those regions (Figs. 7a,b).

The external exchanges with the Pacific and vertical processes in the northern basin determine the middle layer $\overline{\rho_a}$ pattern, which has a positive/negative anomaly in the northern/southern part (Fig. 7a). The horizontal distribution of $\overline{\rho_a}$ (figure not shown) indicates that the intrusion of denser water from the northern part at the depth of the middle layer in LS mainly induces the positive $\overline{\rho_a}$ in the northern basin (Fig. 2b). The upwelling and intensified mixing over the northern slope also has a contribution. Because $\overline{\rho_a}$ represents the spatial anomaly, the negative $\overline{\rho_a}$ occurs over the southern basin as it is farther away from the source of the denser water flowing from LS. In the middle layer, internal upwelling of lighter water over the southern basin (south of 12°N) mainly generates the positive VBF$_M$ (Figs. 7a,b and e). In the northern basin near LS with positive $\overline{\rho_a}$, the upward motion produces the negative VBF$_M$.

In the deep layer, the $\overline{\rho_a}$ has a meridional structure that is opposite to the middle layer's structure where positive $\overline{\rho_a}$ exists over the southern slope, and negative $\overline{\rho_a}$ in the central and northern basin (Fig. 7a). Because the southern slope in the deep layer has a net downwelling (Fig. 7b), the horizontal and vertical advections should not produce the positive $\overline{\rho_a}$ in the deep layer. Instead, the intensified local turbulent mixing processes should produce the positive $\overline{\rho_a}$ there locally (Fig. 7c). Similarly, the positive $\overline{\rho_a}$ in the southern basin, in turn, leads to the negative anomaly in the central basin, where there is a strong upward $\overline{w}$ along the western slope (Fig. 7b). The positive VBF$_M$ in the deep layer maintains the strong eddy-like slope current and is produced by the downwelling of denser water over the southwest corner and the upwelling of lighter water along the western slope (Fig. 7f). Therefore, in the deep layer, the intensified turbulent mixing over the southern slope maintains the density structure and produces the potential energy, which is, in turn, is released by the internal vertical motion.

c. Vertical motion

Under the continuity constraint, the mean vertical motion at depth z is written as (Cai and Gan 2020):

$$\overline{w}(z) = -\nabla_h \cdot \int_{-H}^{z} \overline{\mathbf{V}}_h \, dz \approx -\nabla_h \cdot \int_{-H}^{z} (\overline{\mathbf{V}}_{h\_geo} + \overline{\mathbf{V}}_{h\_adv}) \, dz, \quad (9)$$

in which H is the depth of the bottom topography, and the _geo and _adv represent the geostrophic and nonlinear advection components of the horizontal current, respectively. The effect of the viscosity on the vertical motion is relatively small. The geostrophic component can be expressed as

$$-\nabla_h \cdot \int_{-H}^{z} (\overline{\mathbf{V}}_{h\_geo}) \, dz = \overbrace{-(\overline{v}_{b\_geo} H_y + \overline{u}_{b\_geo} H_x)}^{CGT_b}$$
$$+ \underbrace{\frac{\beta}{f} \int_{-H}^{z} \overline{v}_{geo} \, dz}_{\beta\,effect}, \quad (10)$$

in which the H_x and H_y are the horizontal gradients of the bottom slope. $\overline{u}_{b\_geo}$ and $\overline{v}_{b\_geo}$ are the bottom geostrophic current, and f is the Coriolis parameter. Parameter β is the meridional gradient of f, and $\overline{v}_{geo}$ represents the meridional component of the geostrophic current. By choosing the direction $(x, y) = (x^*, y^*)$ to be the cross- and along-isobath direction, the $\overline{v}_{b\_geo} H_y + \overline{u}_{b\_geo} H_x$ can be further expressed as $\overline{u}^*_{b\_geo} H_{x^*}$, which indicates the bottom cross-isobath geostrophic transport. The two terms on the right side of Eq. (10) represent the cross-isobath geostrophic transport (CGT_b) induced by the pressure gradient force along the isobaths at the bottom (Gan et al. 2013) and the β effect of the meridional geostrophic current below the depth z. The upslope/downslope CGT_b generates an upward/downward motion over the slope according to the bottom kinematic boundary condition and largely contributes to the vertical motion in the deep basin. Thus, the vertical motion $\overline{w}(z)$ in the basin is formed by the bottom cross-isobath geostrophic transport [CGT_b: $-(\overline{v}_{b\_geo} H_y + \overline{u}_{b\_geo} H_x)$], and modified by the beta effect [$(\beta/f)\int_{-H}^{z} \overline{v}_{geo} \, dz$] and nonlinear advection [ADV: $-\nabla_h \cdot \int_{-H}^{z} (\overline{\mathbf{V}}_{h\_adv}) \, dz$] in the water column.

In the upper layer, the CGT_b, beta effect β, and the nonlinear advection (ADV) jointly control the vertical motion (Fig. 8a). While in the middle and deep layers, where the vertical buoyancy flux plays the more important role in forming the basin circulation, the CGT_b largely determines the basic pattern of vertical motion (Figs. 8b,c). In the middle layer, CGT_b cannot explain the $\overline{w}$ in the northern part of the basin, but it should be noted that in the southern basin (south of ~12°N) where there are positive VBF_M and VBF_E, the CGT_b controls the basic upwelling pattern. In the deep layer, the $\overline{w}$ is dominated by the CGT_b that the onshore transport along the western boundary and offshore transport over the southern basin generate the upward and downward motions, respectively.

As illustrated by the layer-integrated vorticity dynamics (Gan et al. 2016a), the bottom pressure torque or the bottom pressure field, which arises from the pressure field (current) interacting with the variable slope topography, is the primary intrinsic response to the external planetary flux. Physically, the
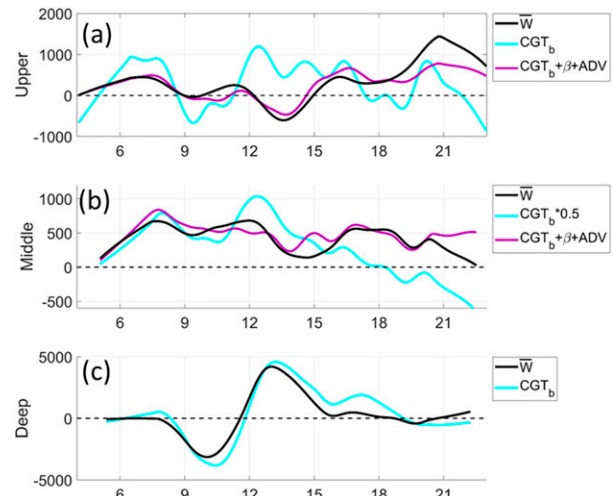

FIG. 8. Zonal- and layer-integrated $\overline{w}$ (black line; m^3 s^{-1}), bottom cross-isobath geostrophic transport (CGT_b) (cyan line; m^3 s^{-1}), and the net vertical motion induced by CGT_b, beta effect and nonlinear advection ($CGT_b + \beta + $ ADV) (purple line; m^3 s^{-1}) as a function of latitude in the upper, middle, and deep layers.

bottom pressure field over the meandering slope topography generates the cross-isobath transport and the vertical motion, particularly in the semi-enclosed deep basin. Similarly, from the perspective of the kinetic energy dynamics, the external forcing in the deep basin does not directly provide the MKE/EKE input, but sets up the large-scale pressure field over the meandering slope topography to generate the vertical motion and release the potential energy for indirectly maintaining the basin circulation.

d. Horizontal pressure work

As shown by Eqs. (5)–(7), the net pressure work (PW$_M$ and PW$_E$) equals the difference between the horizontal pressure work ($\mathbf{V}_h \cdot \nabla_h P_a$) and the vertical buoyancy flux. Figure 9 shows the horizontal pattern of the layer-integrated $\overline{P_a}$, the $\overline{\mathbf{V}}_{VIS}$, and $\overline{\mathbf{V}}_{ADV}$ in the three layers to illustrate how the horizontal pressure work forms. The spatial distributions of the $\overline{P_a}$, $\overline{\mathbf{V}}_{adv}$, and $\overline{\mathbf{V}}_{VIS}$ reflect the characteristics in the forcing processes of the CAC circulation.

In the upper layer (Fig. 9a), the negative $\overline{P_a}$ in the northern basin and along the western boundary represents the mean cyclonic circulation under the geostrophic balance. The dominant annual mean northeast wind forcing produces the prevailing northwestward $\overline{\mathbf{V}}_{VIS}$ through the turbulent viscosity in the upper layer. A stronger $\overline{\mathbf{V}}_{adv}$ generally occurs near LS along the western boundary and southwestern basin where the current is strong and variable. The upper-layer PW_H$_M$, which is negative near LS and positive along the western boundary (Fig. 10a), is mainly formed by the interaction between the local $\overline{\mathbf{V}}_{adv}$ and the $\overline{P_a}$ (Fig. 9a). The $\overline{\mathbf{V}}_{VIS}$ also contributes to the positive pressure work along the western boundary (12°–15°N), but, in general, the $-\overline{\mathbf{V}}_{h\_vis} \cdot \nabla_h \overline{P_a}$ is smaller than $-\overline{\mathbf{V}}_{h\_adv} \cdot \nabla_h \overline{P_a}$. In contrast to PW_H$_M$, the turbulent viscosity plays a relatively important role in forming
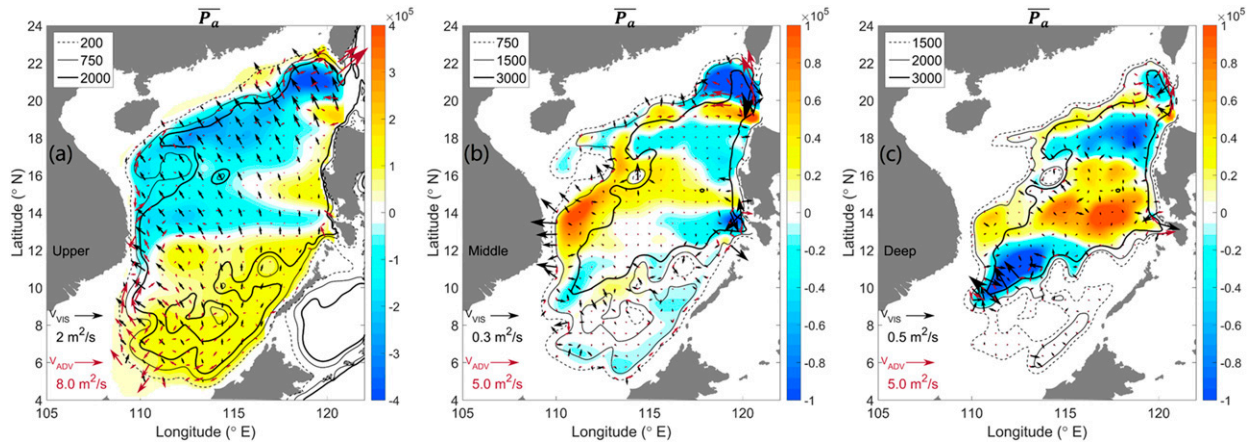
FIG. 9. Horizontal distribution of layer-integrated $\overline{P_a}$ (color contours; Pa) in the (a) upper, (b) middle, and (c) deep layers. Black and red arrows indicate the layer-integrated $\overline{\mathbf{V}}_{\text{VIS}}$ (m² s⁻¹) and $\overline{\mathbf{V}}_{\text{ADV}}$ (m² s⁻¹) in the three layers, respectively.

PW_H$_E$ (Fig. 10d), which is consistent with the dominant contribution of the wind power input by wind stress in the EKE budget.

In the middle layer (Fig. 9b), the strong negative $\overline{P_a}$ near LS shows the local cyclonic gyre induced by the intrusion from the northern part of strait. Associated with the exchanging current, the intensified $\overline{\mathbf{V}}_{\text{adv}}$ forms accordingly. There is positive $\overline{P_a}$ along the western boundary that maintains the mean northward slope current. The onshore $\overline{\mathbf{V}}_{\text{vis}}$ at the western boundary, which flows from high $\overline{P_a}$ to low $\overline{P_a}$, represents the turbulent viscosity in the cyclonic direction induced by the bottom friction of the anticyclonic slope current (Fig. 9b). Meridionally, the positive PW_H$_M$ that supports the high MKE is mainly produced by the nonlinearity near LS (18°–21°N) and by $\overline{\mathbf{V}}_{\text{vis}}$ along the western slope (Fig. 10b). For the total middle layer MKE budget, the turbulent viscosity mainly contributes to the PW_H$_M$. Similarly, the $\overline{\mathbf{V}}_{\text{vis}}$ dominates the PW_H$_E$. As we

described earlier, the intensity of the turbulent mixing is elevated near LS and over the basin slope due to the enormous energy dissipation of internal tides and eddies (e.g., Tian et al. 2009; Yang et al. 2014; Wang et al. 2016; Yang et al. 2019). The intensified mixing and the induced perturbation in the pressure field contribute largely to the PW_H$_E$, which generates high values in the northern basin (18°–21°N) and along the western slope (~12°N) to maintain the high EKE there (Fig. 10e).

The deep layer $\overline{P_a}$ has a negative–positive–negative pattern from the northern to the southern basin (Fig. 9c), which suggests that the deep circulation is divided into three sections: a weak cyclonic circulation in the northern SCS, a weak anticyclonic circulation in the eastern SCS, and a strong cyclonic circulation over the southwest corner. Similarly, the relatively larger $\overline{\mathbf{V}}_{\text{adv}}$ forms near LS in the northern basin associated with the deep intrusion. The offshore $\overline{\mathbf{V}}_{\text{vis}}$ occurs over the southwest corner, as the result of the bottom friction of the cyclonic slope
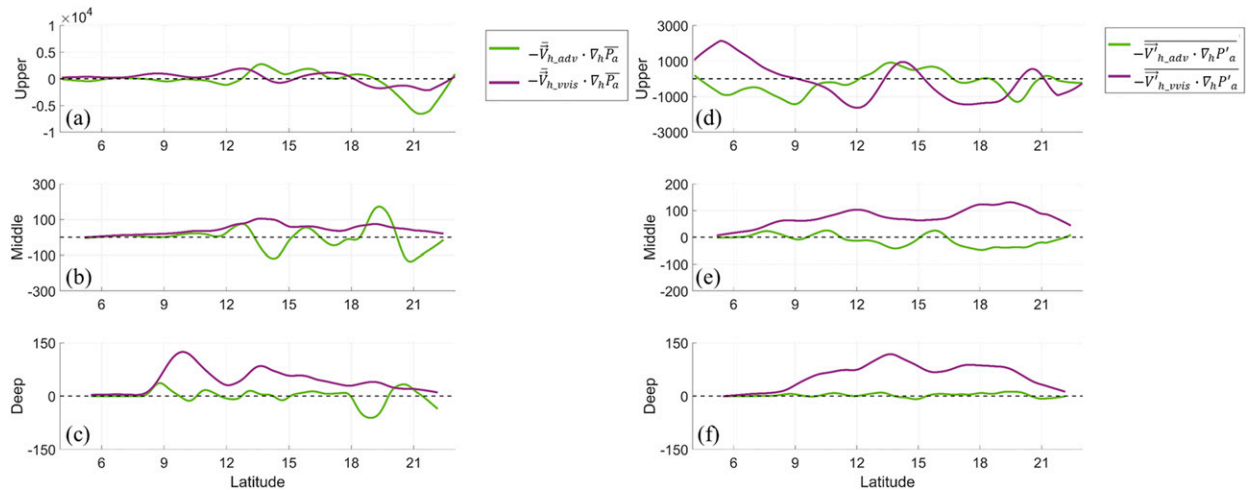

FIG. 10. (a)–(c) Zonal- and layer-integrated $-\overline{\mathbf{V}}_{h\_\text{adv}} \cdot \nabla_h \overline{P_a}$ (J m⁻¹ s⁻¹) and $-\overline{\mathbf{V}}_{h\_\text{vvis}} \cdot \nabla_h \overline{P_a}$ (J m⁻¹ s⁻¹) in the three layers. (d)–(f) As in (a)–(c), but for $-\overline{\mathbf{V}'_{h\_\text{adv}} \cdot \nabla_h P'_a}$ (J m⁻¹ s⁻¹) and $\overline{-\mathbf{V}'_{h\_\text{vvis}} \cdot \nabla_h P'_a}$ (J m⁻¹ s⁻¹).
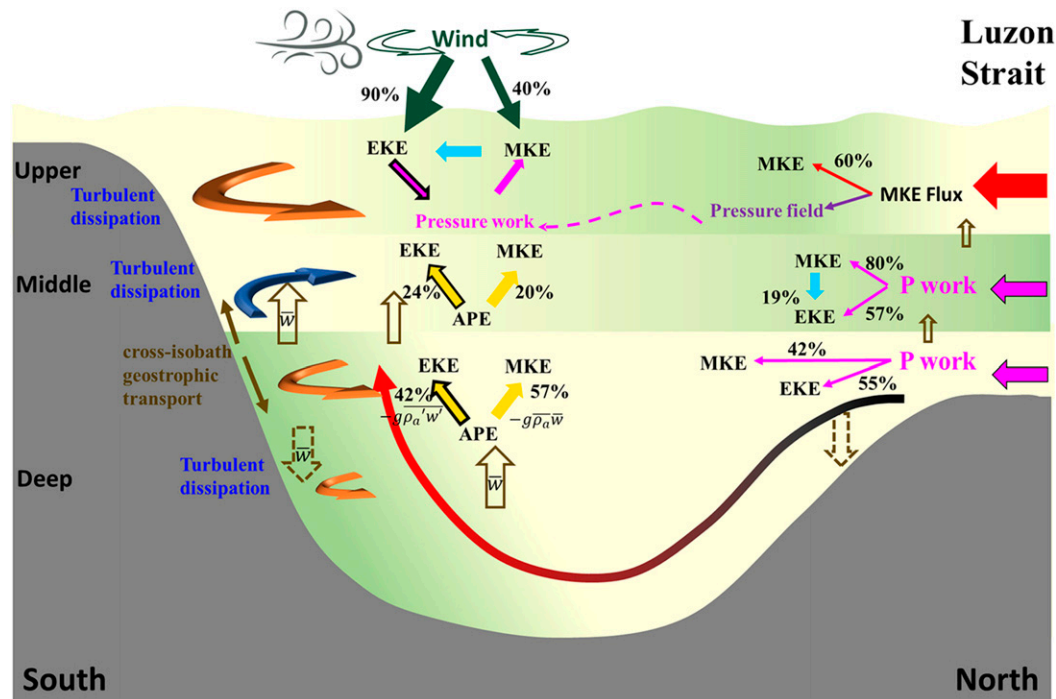
FIG. 11. Conceptual diagram to illustrate the formation dynamics of the CAC circulation inferred from kinetic energy pathway. The background color represents the mean density anomaly pattern in the three layers. Percentages show the contribution to MKE or EKE from respective sources in each layer.

current, and produces the high PW_H$_M$ there (Fig. 10c). Same as the middle layer the generation of high PW_H$_E$ in the central basin (12°–15°) and northern basin (~18°N) is dominated by the turbulent viscosity (Fig. 10f), which is also contributed by the internal tide induced intensified mixing and the perturbations in the pressure field.

As illustrated in section 5a, in the middle and deep layers, the local vertical buoyancy flux generates the positive baroclinic instability (VBF$_E$ and VBF$_M$) along the western boundary and in the southern basin. Because of the hydrostatic condition $[-g\rho_a w = w(\partial P_a / \partial z)]$, the local upward vertical buoyancy flux induces the negative vertical pressure work in these two layers, which, in turn, cancels the high horizontal pressure work (PW_H$_M$ and PW_H$_E$). Thus, the net pressure work (PW$_M$ and PW$_E$) mainly affects the circulation in the northern basin, and the internal baroclinic instability induced by the vertical buoyancy flux contributes to the strong slope current and EKE inside the basin (Fig. 5).

6. Summary

Using the results from the validated CMOMS, this study presents a full three-dimensional picture of the characteristics and pathway of kinetic energy in the CAC circulation of the SCS. Using an analysis of the energetics in the system, we provided a new insight into the maintenance of CAC circulation associated with the coupled external forcing and internal responses as well as with the interaction between the geostrophic motion and ageostrophic processes in the SCS.

The MKE exists along the basin slope and represents the structure and intensity of the mean CAC circulation. In the upper and middle layers, strong MKE is found in the northern basin near LS (18°–21°N) affected by flow exchange with the Pacific and along the western slope (12°–15°N) with steep and narrow topography. In the deep layer, the strong eddy-like slope current over the topographic trough at the southwest corner mainly generates the MKE. The EKE distribution is not the same as the MKE's distribution but is strongly affected by the vertical shear and stratification in the mean circulation, particularly in the semi-enclosed middle and deep layers.

In the three layers of the CAC circulation, the geostrophic balance dominates the MKE and EKE, and the ageostrophic components are found mainly along the western slope where there are a strong boundary current and steep topography, and in the northern basin near LS, where there are an external exchanging current, enormous eddy activities, and strong internal tides. In the upper layer, the larger ageostrophic component of the EKE also exists in the southwestern basin, which is affected by the seasonal reversing circulation and eddies associated with coastal current separation. The intensity of the ageostrophic motion is much weaker than the intensity of the geostrophic motion but largely modulates the energy dynamics of the CAC circulation.

The kinetic energy pathway pattern in the CAC circulation is summarized in the conceptual diagram in Fig. 11. In the upper layer, the MKE input from the Kuroshio intrusion (60%) and the wind forcing (40%) drive the mean cyclonic circulation, which produces the high MKE near LS and along

the western boundary, and the upper-layer acquires the most EKE from the wind (90%) through the turbulent viscosity induced wind stress. The strong nonlinear interaction between the mean and eddy flow converts MKE to EKE over the southern basin to cascade the energy of the mean circulation. The net contributions from the pressure work and vertical buoyancy flux are relatively limited in the upper-layer circulation.

In the semi-enclosed middle layer, the external forcing does not directly provide the MKE and EKE of the anticyclonic circulation. It is the internal pressure work in the northern basin near LS (80% for MKE and 57% for EKE) and the vertical buoyancy flux in the southern basin and along the western slope (20% for MKE and 24% for EKE) that maintain the MKE and EKE in the middle layer, which involves the interaction between the geostrophic and ageostrophic processes. Over the northern slope, the EKE also extracts energy from the mean circulation through nonlinear interaction.

Similarly, in the deep layer, the release of the APE through internal VBF_M (57%) locally maintains the cyclonic slope current over the southwest corner. The PW_E (55%) and local VBF_E (42%) produce the high EKE in the northern basin and central basin, respectively.

In the CAC circulation, the large-scale internal vertical motion associated with the bottom pressure torque determines the vertical buoyancy flux (VBF_M and VBF_E) and is the primary intrinsic response to the external forcing through LS and the density field maintained by internal mixing and the external current exchange. Thus, for the circulation in the semi-enclosed middle and deep layers, the external forcing sets up the large-scale pressure field over the meandering continental slope to generate the vertical motion and release the potential energy that indirectly maintains the basin circulation. The upwelling over the southern basin provides the release of APE in the middle layer. However, in the deep layer, the downwelling of denser water over the southwest corner and the upwelling of the lighter water over the western boundary release the APE.

The horizontal pressure work and the vertical buoyancy flux determine the net pressure work, and the interaction between the pressure field and the turbulent viscosity mainly generates the horizontal pressure work. In the semi-enclosed middle and deep layers, the local vertical buoyancy flux cancels the large horizontal pressure work along the western boundary and in the southern basin. Thus, the net pressure work (PW_M and PW_E) mainly affects the current in the northern basin near LS. The kinetic energy pathway in the CAC circulation indicates that the external forcing dominates upper-layer circulation and the coupling between internal and external dynamics is crucial for maintaining the circulation in the middle and deep layers.

REFERENCES

Alford, M. H., and Coauthors, 2015: The formation and fate of internal waves in the South China Sea. *Nature*, **521**, 65–69, https://doi.org/10.1038/nature14399.

Cai, Z., and J. Gan, 2019: Coupled external-internal dynamics of layered circulation in the South China Sea: A modeling study. *J. Geophys. Res. Oceans*, **124**, 5039–5053, https://doi.org/10.1029/2019JC014962.

——, and ——, 2020: Dynamics of the cross-layer exchange for the layered circulation in the South China Sea. *J. Geophys. Res. Oceans*, **125**, e2020JC016131, https://doi.org/10.1029/2020JC016131.

Cessi, P., N. Pinardi, and V. Lyubartsev, 2014: Energetics of semienclosed basins with two-layer flows at the strait. *J. Phys. Oceanogr.*, **44**, 967–979, https://doi.org/10.1175/JPO-D-13-0129.1.

Chang, M.-H., R.-C. Lien, T. Y. Tang, E. A. D'Asaro, and Y. J. Yang, 2006: Energy flux of nonlinear internal waves in northern South China Sea. *Geophys. Res. Lett.*, 33, L03607, https://doi.org/10.1029/2005GL025196.

Chen, G., Y. Hou, X. Chu, and P. Qi, 2009: The variability of eddy kinetic energy in the South China Sea deduced from satellite altimeter data. *Chin. J. Oceanology Limnol.*, **27**, 943–954, https://doi.org/10.1007/s00343-009-9297-6.

Chen, R., A. F. Thompson, and G. R. Flierl, 2016: Time-dependent eddy-mean energy diagrams and their application to the ocean. *J. Phys. Oceanogr.*, **46**, 2827–2850, https://doi.org/10.1175/JPO-D-16-0012.1.

Cheng, X. H., and Y. Q. Qi, 2010: Variations of eddy kinetic energy in the South China Sea. *J. Oceanogr.*, **66**, 85–94, https://doi.org/10.1007/s10872-010-0007-y.

Fang, G., Y. Wang, Z. Wei, Y. Fang, F. Qiao, and X. Hu, 2009: Interocean circulation and heat and freshwater budgets of the South China Sea based on a numerical model. *Dyn. Atmos. Oceans*, **47**, 55–72, https://doi.org/10.1016/j.dynatmoce.2008.09.003.

Ferrari, R., and C. Wunsch, 2009: Ocean circulation kinetic energy: Reservoirs, sources, and sinks. *Annu. Rev. Fluid Mech.*, **41**, 253–282, https://doi.org/10.1146/annurev.fluid.40.111406.102139.

Gan, J., and T. Qu, 2008: Coastal jet separation and associated flow variability in the southwest South China Sea. *Deep-Sea Res. I*, **55**, 1–19, https://doi.org/10.1016/j.dsr.2007.09.008.

——, H. Li, E. N. Curchitser, and D. B. Haidvogel, 2006: Modeling South China sea circulation: Response to seasonal forcing regimes. *J. Geophys. Res. Oceans*, **111**, C06034, https://doi.org/10.1029/2005JC003298.

——, H. San Ho, and L. Liang, 2013: Dynamics of intensified downwelling circulation over a widened shelf in the northeastern South China Sea. *J. Phys. Oceanogr.*, **43**, 80–94, https://doi.org/10.1175/JPO-D-12-02.1.

——, Z. Liu, and C. R. Hui, 2016a: A three-layer alternating spinning circulation in the South China Sea. *J. Phys. Oceanogr.*, **46**, 2309–2315, https://doi.org/10.1175/JPO-D-16-0044.1.

——, ——, and L. Liang, 2016b: Numerical modeling of intrinsically and extrinsically forced seasonal circulation in the China Seas: A kinematic study. *J. Geophys. Res. Oceans*, **121**, 4697–4715, https://doi.org/10.1002/2016JC011800.

Greatbatch, R. J., X. Zhai, M. Claus, L. Czeschel, and W. Rath, 2010: Transport driven by eddy momentum fluxes in the Gulf Stream Extension region. *Geophys. Res. Lett.*, **37**, L24401, https://doi.org/10.1029/2010GL045473.

Huang, X., Z. Chen, W. Zhao, Z. Zhang, C. Zhou, Q. Yang, and J. Tian, 2016: An extreme internal solitary wave event observed in the northern South China Sea. *Sci. Rep.*, **6**, 30041, https://doi.org/10.1038/srep30041.

Kang, D., and E. N. Curchitser, 2015: Energetics of eddy–mean flow interactions in the Gulf Stream region. *J. Phys. Oceanogr.*, **45**, 1103–1120, https://doi.org/10.1175/JPO-D-14-0200.1.

Lan, J., N. Zhang, and Y. Wang, 2013: On the dynamics of the South China Sea deep circulation. *J. Geophys. Res. Oceans*, **118**, 1206–1210, https://doi.org/10.1002/jgrc.20104.

——, Y. Wang, F. Cui, and N. Zhang, 2015: Seasonal variation in the South China Sea deep circulation. *J. Geophys. Res. Oceans*, **120**, 1682–1690, https://doi.org/10.1002/2014JC010413.

Liu, Z., and J. Gan, 2016: Open boundary conditions for tidally and subtidally forced circulation in a limited-area coastal model using the Regional Ocean Modeling System (ROMS). *J. Geophys. Res. Oceans*, **121**, 6184–6203, https://doi.org/10.1002/2016JC011975.

——, and ——, 2017: Three-dimensional pathways of water masses in the south China Sea: A modeling study. *J. Geophys. Res. Oceans*, **122**, 6039–6054, https://doi.org/10.1002/2016JC012511.

Magalhães, F. C., J. L. L. Azevedo, and L. R. Oliveira, 2017: Energetics of eddy-mean flow interactions in the Brazil Current between 20°S and 36°S. *J. Geophys. Res. Oceans*, **122**, 6129–6146, https://doi.org/10.1002/2016JC012609.

Masumoto, Y., H. Sasaki, T. Kagimoto, and N. Komori, 2004: A fifty-year eddy-resolving simulation of the world ocean–preliminary outcomes of OFES (OGCM for the Earth Simulator). *J. Earth Simul.*, **1**, 35–56.

Mellor, G. L., and T. Yamada, 1982: Development of a turbulence closure model for geophysical fluid problems. *Rev. Geophys. Space Phys.*, **20**, 851–875, https://doi.org/10.1029/RG020i004p00851.

Nan, F., H. Xue, and F. Yu, 2015: Kuroshio intrusion into the South China Sea: A review. *Prog. Oceanogr.*, **137**, 314–333, https://doi.org/10.1016/j.pocean.2014.05.012.

Noh, Y., B. Y. Yim, S. H. You, J. H. Yoon, and B. Qiu, 2007: Seasonal variation of eddy kinetic energy of the North Pacific Subtropical Countercurrent simulated by an eddy-resolving OGCM. *Geophys. Res. Lett.*, **34**, L07601, https://doi.org/10.1029/2006GL029130.

Qiu, B., 1999: Seasonal eddy field modulation of the North Pacific subtropical countercurrent: TOPEX/Poseidon observations and theory. *J. Phys. Oceanogr.*, **29**, 2471–2486, https://doi.org/10.1175/1520-0485(1999)029<2471:SEFMOT>2.0.CO;2.

Qu, T., J. B. Girton, and J. A. Whitehead, 2006: Deepwater overflow through Luzon Strait. *J. Geophys. Res.*, **111**, C01002, https://doi.org/10.1029/2005JC003139.

——, Y. T. Song, and T. Yamagata, 2009: An introduction to the South China Sea throughflow: Its dynamics, variability, and application for climate. *Dyn. Atmos. Oceans*, **47**, 3–14, https://doi.org/10.1016/j.dynatmoce.2008.05.001.

Quan, Q., and H. Xue, 2018: Layered model and insights into the vertical coupling of the South China Sea circulation in the upper and middle layers. *Ocean Modell.*, **129**, 75–92, https://doi.org/10.1016/j.ocemod.2018.06.006.

——, and ——, 2019: Influence of abyssal mixing on the multilayer circulation in the South China Sea. *J. Phys. Oceanogr.*, **49**, 3045–3060, https://doi.org/10.1175/JPO-D-19-0020.1.

Richardson, P. L., 1983: Eddy kinetic energy in the North Atlantic from surface drifters. *J. Geophys. Res.*, **88**, 4355–4367, https://doi.org/10.1029/JC088iC07p04355.

Shchepetkin, A. F., and J. C. McWilliams, 2005: The Regional Ocean Modeling System (ROMS): A split-explicit, free-surface, topography following coordinates ocean model. *Ocean Modell.*, **9**, 347–404, https://doi.org/10.1016/j.ocemod.2004.08.002.

Shu, Y., H. Xue, D. Wang, F. Chai, Q. Xie, J. Yao, and J. Xiao, 2014: Meridional overturning circulation in the South China Sea envisioned from the high-resolution global reanalysis data GLBa0.08. *J. Geophys. Res. Oceans*, **119**, 3012–3028, https://doi.org/10.1002/2013JC009583.

Stammer, D., 1997: Global characteristics of ocean variability estimated from regional TOPEX/Poseidon altimeter measurements. *J. Phys. Oceanogr.*, **27**, 1743–1769, https://doi.org/10.1175/1520-0485(1997)027<1743:GCOOVE>2.0.CO;2.

Su, J., 2004: Overview of the South China Sea circulation and its influence on the coastal physical oceanography outside the Pearl River Estuary. *Cont. Shelf Res.*, **24**, 1745–1760, https://doi.org/10.1016/j.csr.2004.06.005.

Tian, J., Q. Yang, and W. Zhao, 2009: Enhanced diapycnal mixing in the South China Sea. *J. Phys. Oceanogr.*, **39**, 3191–3203, https://doi.org/10.1175/2009JPO3899.1.

Wang, G., J. Su, and P. C. Chu, 2003: Mesoscale eddies in the South China Sea observed with altimeter data. *Geophys. Res. Lett.*, **30**, 2121, https://doi.org/10.1029/2003GL018532.

——, S.-P. Xie, T. Qu, and R. X. Huang, 2011: Deep South China Sea circulation. *Geophys. Res. Lett.*, **38**, L05601, https://doi.org/10.1029/2010GL046626.

Wang, H., D. Wang, G. Liu, H. Wu, and M. Li, 2012: Seasonal variation of eddy kinetic energy in the South China Sea. *Acta Oceanol. Sin.*, **31**, 1–15, https://doi.org/10.1007/s13131-012-0170-7.

Wang, X., S. Peng, Z. Liu, R. X. Huang, Y. K. Qian, and Y. Li, 2016: Tidal mixing in the South China Sea: An estimate based on the internal tide energetics. *J. Phys. Oceanogr.*, **46**, 107–124, https://doi.org/10.1175/JPO-D-15-0082.1.

——, Z. Liu, and S. Peng, 2017: Impact of tidal mixing on water mass transformation and circulation in the South China Sea. *J. Phys. Oceanogr.*, **47**, 419–432, https://doi.org/10.1175/JPO-D-16-0171.1.

Wyrtki, K., L. Magaard, and J. Hager, 1976: Eddy energy in the oceans. *J. Geophys. Res.*, **81**, 2641–2646, https://doi.org/10.1029/JC081i015p02641.

Xu, F.-H., and L.-Y. Oey, 2014: State analysis using the local ensemble transform Kalman filter (LETKF) and the three-layer circulation structure of the Luzon Strait and the South China Sea. *Ocean Dyn.*, **64**, 905–923, https://doi.org/10.1007/s10236-014-0720-y.

Xu, Z., K. Liu, B. Yin, Z. Zhao, Y. Wang, and Q. Li, 2016: Long-range propagation and associated variability of internal tides in the South China Sea. *J. Geophys. Res. Oceans*, **121**, 8268–8286, https://doi.org/10.1002/2016JC012105.

Xue, H., F. Chai, N. Pettigrew, D. Xu, M. Shi, and J. Xu, 2004: Kuroshio intrusion and the circulation in the South China Sea. *J. Geophys. Res. Oceans*, **109**, C02017, https://doi.org/10.1029/2002JC001724.

Yang, H., Q. Liu, Z. Liu, D. Wang, and X. Liu, 2002: A general circulation model study of the dynamics of the upper ocean

circulation of the South China Sea. *J. Geophys. Res.*, **107**, 3085, https://doi.org/10.1029/2001JC001084.

——, L. Wu, H. Liu, and Y. Yu, 2013: Eddy energy sources and sinks in the South China Sea. *J. Geophys. Res. Oceans*, **118**, 4716–4726, https://doi.org/10.1002/jgrc.20343.

Yang, J., and J. F. Price, 2000: Water-mass formation and potential vorticity balance in an abyssal ocean circulation. *J. Mar. Res.*, **58**, 789–808, https://doi.org/10.1357/002224000321358918.

Yang, Q., J. Tian, W. Zhao, X. Liang, and L. Zhou, 2014: Observations of turbulence on the shelf and slope of northern South China Sea. *Deep-Sea Res. I*, **87**, 43–52, https://doi.org/10.1016/j.dsr.2014.02.006.

——, M. Nikurashin, H. Sasaki, H. Sun, and J. Tian, 2019: Dissipation of mesoscale eddies and its contribution to mixing in the northern South China Sea. *Sci. Rep.*, **9**, 556, https://doi.org/10.1038/s41598-018-36610-x.

Yuan, D., 2002: A numerical study of the South China Sea deep circulation and its relation to the Luzon Strait transport. *Acta Oceanol. Sin.*, **21**, 187–202.

Zhang, Z., W. Zhao, B. Qiu, and J. Tian, 2017: Anticyclonic eddy sheddings from Kuroshio loop and the accompanying cyclonic eddy in the northeastern South China Sea. *J. Phys. Oceanogr.*, **47**, 1243–1259, https://doi.org/10.1175/JPO-D-16-0185.1.

Zhao, W., C. Zhou, J. Tian, Q. Yang, B. Wang, L. Xie, and T. Qu, 2014: Deep water circulation in the Luzon Strait. *J. Geophys. Res. Oceans*, **119**, 790–804, https://doi.org/10.1002/2013JC009587.

Zhu, Y., J. Sun, Y. Wang, Z. Wei, D. Yang, and T. Qu, 2017: Effect of potential vorticity flux on the circulation in the South China Sea. *J. Geophys. Res. Oceans*, **122**, 6454–6469, https://doi.org/10.1002/2016JC012375.

——, ——, ——, S. Li, T. Xu, Z. Wei, and T. Qu, 2019: Overview of the multi-layer circulation in the South China Sea. *Prog. Oceanogr.*, **175**, 171–182, https://doi.org/10.1016/j.pocean.2019.04.001.

Zu, T., J. Gan, and S. Erofeeva, 2008: Numerical study of the tide and tidal dynamics in the South China Sea. *Deep-Sea Res. I*, **55**, 137–154, https://doi.org/10.1016/j.dsr.2007.10.007.